This is a “preproof” accepted article for *Mineralogical Magazine*.
This version may be subject to change during the production process.
10.1180/mgm.2025.11

REV1

Mineralogy and geochemistry of pattern formation in print stone from the Pilbara, Australia

Andrew J Coward[1], Joël Brugger[1,*], Sasha Wilson[2], Anja C Slim[1], Tim Williams[3], Brad Pillans[4], Anton Maksimenko[5]

[1]*School of Earth, Atmosphere and Environment, Monash University, Clayton, VIC 3800, Australia*

[2]*Department of Earth and Atmospheric Sciences, University of Alberta, Edmonton, AB T6G 2R3, Canada*

[3]*Monash Centre for Electron Microscopy, Monash University, Clayton, VIC 3800, Australia*

[4]*Research School of Earth Sciences, Australian National University, Canberra, ACT 2601, Australia*

[5]*Australian Synchrotron (ANSTO), Clayton, VIC 3168, Australia*

* Corresponding author email: joel.brugger@monash.edu

Abstract

‘Print stone’ is an iron-banded siltstone from the Pilbara Province of Western Australia that bears partial resemblance to iconic East Kimberley ‘zebra rock’ in both pattern morphology and mineralogical composition. Using a combination of mineralogy and elemental geochemistry, this study examines the mechanisms underlying the formation of periodic iron-oxide banding in print stone. We demonstrate that print stone patterns likely arose from the periodic deposition of hydrothermal pyrite during the early Paleoproterozoic, as evidenced by the distinctive cuboid morphology of the hematite pigment, the deposition of iron oxides along fluid-transport pathways, the presence of extensive hydrothermal pyrite elsewhere in the formation, and the presence of a positive europium anomaly. Through spatial analysis of the iron-oxide banding, we further show that print stone adheres to the Liesegang spacing law with a spacing coefficient of 0.018. This suggests that the periodic

https://doi.org/10.1180/mgm.2025.11 Published online by Cambridge University Press

deposition of pyrite in print stone arose due to the Liesegang phenomenon, which was likely triggered by the infiltration of near-neutral, sulfidic hydrothermal fluids into a ferruginous, feldspathic shale. Altogether, the findings of this study demonstrate the ability for iron-oxide Liesegang bands to develop in hydrothermal systems, providing additional insight into the mechanisms underlying the formation of East Kimberley zebra rock and other banded geological material.

Keywords: print stone, zebra rock, Liesegang banding, pattern formation, Mount McRae Shale.

1. Introduction

Pattern formation within rocks and minerals involves the nonhomogeneous arrangement of chemical species into spatial structures. These structures have long been a subject of research in the geosciences, where they can be observed at every scale, from the cyclic, stratigraphic variations in kilometre-scale outcrops of interbedded sandstone and shale (Paulissen and Luthi, 2011), down to the µm-sized zoning within single crystals (Shore and Fowler, 1996; Perugini *et al.*, 2006).

Several prominent examples of geological pattern formation can be found in the north and north-western districts of Western Australia, including banded iron formations (e.g., Klein, 2005) and 'zebra rock' (e.g., Coward *et al.*, 2023). Zebra rock rock is famous for its distinctive periodic iron-oxide pattern, which transforms an Ediacaran-aged siltstone into an attractive semi-precious gemstone. Zebra rock has been the subject of a number of recent studies, with pattern formation ascribed to either pedogenic redoximorphic features or Liesegang banding (Abrajevitch *et al.*, 2018; Retallack, 2020; Kawahara *et al.*, 2022; Coward *et al.*, 2023; Yatsuda *et al.*, 2023). Although zebra rock has only ever been identified around the vicinity of Lake Argyle in Western Australia, comparable rhythmic Fe-oxide patterns are also observed in siltstones located across the neighbouring Pilbara region. These patterns are referred to as either 'print stone' or 'newsprint jasper', and are located within the upper section of the Neoarchean to Early Paleoproterozoic (2494–2505 Ma) Mount McRae Shale. The Mount McRae Shale has been of significant interest to the academic community over the past few decades, due in part to the extensive history of hydrothermal iron mineralisation throughout the region (e.g., Rasmussen *et al.*, 2007; Reinhard *et al.*, 2009; Raiswell *et al.*, 2011); the economic significance of the overlying Brockman Iron Formation (e.g., Haruna *et*

https://doi.org/10.1180/mgm.2025.11 Published online by Cambridge University Press

al., 2003); and the possible preservation of evidence of trace oxygen hundreds of millions of years prior to the Great Oxygenation Event (Anbar et al. 2007; Slotznick *et al.*, 2022). However, despite extensive mineralogical and isotopic analysis of the host formation, print stone has not yet been examined outside of its paleomagnetic properties, which served to date the formation of the iron-oxide pigment to either ~1.5 Ga or ~310–320 Ma (Abrajevitch *et al.*, 2014).

Although less renowned than the unusual hematite patterns that define zebra rock, the distinctive iron-oxide banding of print stone (Fig. 1) nonetheless shares many of the same physical characteristics, including a well-defined, spatially repeating pattern and the occurrence of spot- and rod-like pattern morphologies. However, unlike zebra rock, print stone patterns also exhibit clear and linear variabilities in the width and spacing of its bands (Fig. 1), in a fashion reminiscent of the scaling laws that define Liesegang banding. Liesegang banding is a phenomenon observed in certain reaction-diffusion systems, whereby a migrating chemical front results in the precipitation of alternating bands or rings (e.g., Hartman and Dickey, 1932; Yatsuda *et al.*, 2023). Laboratory and field observations of Liesegang banding have shown that spacing and width of the bands are bound by specific rules, collectively called 'scaling laws'. The spacing law describes the successive linear increases in interband spacing with increasing distance from the pattern origin point (Jablczynski, 1923), while the width law states that the width of the n^{th} band is proportional to a positive power of its distance from the origin point (Müller *et al.*, 1982). The spacing and width laws can be described through the following equations respectively:

$$\lim_{n\to\infty}(x_{n+1}/x_n) = 1 + p \qquad (1)$$

$$w_n \propto x_n^a \qquad (2)$$

where x_n is the distance of the n^{th} band from the origin point, w_n is its width, p is the spacing coefficient, and a is a unitless parameter with a value close to unity (Droz *et al.*, 1999).

The geological collocation of print stones and zebra rocks provides an opportunity to gain further insights into the formation and geological significance of periodic iron-oxide banding. Extensive mineralogical and geochemical data were obtained for multiple print stone samples sourced from three different localities in order to characterise the mineralogical and geochemical features of print stone and constrain the mechanism of self-organisation by which its patterns were formed. The pattern morphology of print stone was examined by spatial analysis, for the purpose of confirming the occurrence of the Liesegang phenomenon. This information was used to construct a possible pathway for the formation of hematite

https://doi.org/10.1180/mgm.2025.11 Published online by Cambridge University Press

patterns in print stone that is consistent with all established physical and geochemical constraints, as well as providing crucial insights into the origin of the hematite banding in East Kimberley zebra rock.

2. Geological context

All known print stone outcrops are located within the Neoarchean to Early Paleoproterozoic, 2500 m thick Hamersley Group, which was deposited between 2.45 to 2.63 Ga ago as part of the Mt Bruce Supergroup (Trendall *et al.*, 2004). The Hamersley group is subdivided into eight formations, composed of shales, dolomites, dolerites, rhyolites and banded iron formations (BIFs), the largest and most economically significant of which are the *Marra Mamba Iron Formation* and the *Brockman Iron Formation* (Trendall and Blockley, 1970). Separating these two BIF units are, in younging order: the dolomites and cherts of the *Wittenoom formation*; *Mount Sylvia* cherts and interbedded shales; and the shales and siltstones of the *Mount McRae Shale*, the latter two units being merged into the '*Mount McRae Shale and Mount Sylvia Formation*' (Fig. 2; Trendall and Blockley, 1970; Thorne and Tyler, 1997).

The print stone-hosting Mount McRae Shale is a carbonaceous, marine shale with a conformable boundary with the underlying Mount Sylvia unit defined by a distinctive BIF marker bed termed 'Bruno's band'. The Mount McRae Shale has been well studied, in part due to the possibility that it may preserve evidence of an early rise in atmospheric oxygen in the form of localised Mo and Re enrichments and sulfur isotope anomalies (Anbar *et al.*, 2007; Kaufman *et al.*, 2007). The Mount McRae Shale was deposited approximately 2.50 Ga ago, as determined by ^{207}Pb – ^{206}Pb zircon dating (Rasmussen *et al.*, 2005). It consists of interbedded chert, shale, carbonates, and sideritic BIFs, with quartz, K-feldspar, sericite, and chlorite present throughout as the major mineral phases, alongside varying amounts of carbonates (e.g., siderite, dolomite, ankerite) and pyrite (Trendall and Blockley, 1970; Raiswell *et al.*, 2011), with the latter present both as larger nodules formed during burial diagenesis, and smaller, euhedral crystals formed through hydrothermal mineralization (Haruna *et al.*, 2003; Slotznick *et al.*, 2022).

The top of the Mount McRae Shale unit is defined by a black shale bed half a metre thick, directly underlying the lowest BIF band of the Brockman Iron Formation (Trendall and Blockley, 1970). The Brockman Iron Formation contains some of the highest-grade hematite ore deposits in the world, likely formed via upgrading of BIF through repeated circulation of hydrothermal fluids along major fault lines, beginning approximately 2.15 Ga ago with

https://doi.org/10.1180/mgm.2025.11 Published online by Cambridge University Press

subsequent hydrothermal alteration reoccurring on at least seven more occasions over the next 1.3 billion years (Rasmussen *et al.*, 2007).

Samples were sourced from three print stone outcrops across the Pilbara (Fig. 2). Localities include an existing mining lease at *Hamersley Ridge*, as well as two previously undocumented outcrops, labelled according to nearby geographical features as *Wittenoom* and *Great Northern Highway* (Fig. 3).

3. Analytical methods

A range of analytical techniques were used to characterise the mineralogy, textures, and geochemistry of rocks, including powder X-ray diffraction (XRD), scanning electron microscopy (SEM), synchrotron-based X-ray fluorescence microscopy (XFM), and synchrotron-based X-ray tomography. For further information regarding the methodology of these analyses, refer to the analytical methods of Coward *et al.* (2023).

To determine whether print stone banding is consistent with the spacing and width laws inherent in Liesegang banding, spatial analysis of print stone was conducted on a sample from Wittenoom with vertical to near-vertical banding orientated perpendicular to bedding. This criterion was necessary due to variations in grain size and mineralogy observed along the vertical axis of most print stone beds, which are both parameters predicted to provide additional controls on the spacing and width of print stone bands and prevent accurate calculation of a spacing coefficient. No samples meeting this criterion could be retrieved from the Hamersley Ridge or Great Northern Highway deposits.

The sample was cut open orthogonal to the direction of band propagation. A line of known length was drawn across the image parallel to bedding, intersecting the pattern at a height where the banding was deemed closest to vertical, without any significant forking or discontinuations. Images of the cut, patterned sample were first processed using ImageJ (Abramoff *et al.*, 2004), subtracting the background, and setting a threshold colour value in order to highlight the dark and light banding. The band width (w_n) was defined by the points in which the line crossed the predetermined threshold colour value. Likewise, x_n was defined by the length along the line from the edge of the sample to the centre of the band, as defined by the colour threshold. In all samples, the origin was chosen so that x_n would increase in the direction of increasing interband spacing. To determine if banded print stone patterns adhered to the spacing law, a least-squares linear-regression was applied to a plot of x_{n+1} against x_n, with the reported gradient of the regression approximating the apparent spacing coefficient of the patterned sample. Similarly, the degree of consistency of print stone to the width law was

https://doi.org/10.1180/mgm.2025.11 Published online by Cambridge University Press

determined by a least-squares linear-regression of a plot of x_n against w_n. A t-test was performed on both regressions to obtain a measure of significance (P>0.01). All linear-regressions and associated t-tests were undertaken using RStudio.

4. Results

4.1. Pattern morphology

Print stone patterns were observed *in-situ* at all three outcrops as discrete layers of discontinuous banded structures (expressed as sheets in three dimensions; Fig. 4), with spot-like morphologies also observed (Fig. 3, bottom). Print stone banding showed a high variability in bandwidth (ranging from <1 mm to 10 mm) and band-spacing at both outcrop and hand-sample scales and possessed a high frequency of band-splitting and band discontinuities, particularly in comparison to zebra rock. Also, unlike zebra rock, print stone patterns regularly extended vertically into adjacent bedding, with the pattern wavelength changing across vertical strata (Fig. 5). Pattern morphology was, in some sections, strongly influenced by intercutting vertical joints and faults, leading to the development of distinctive, concentric ring-like structures (Fig. 5). At Wittenoom, the distribution of the iron-oxide pigment was also preferentially located along horizontal laminations, which could be observed in the XFM images of Fe in samples from this deposit (Fig. 6A). This phenomenon was not present at Hamersley Ridge or Great Northern Highway, as the patterned siltstone beddings at these locations were predominately massive in character.

At the Hamersley Ridge outcrop, a secondary pattern was observed overprinting the primary pigment (Fig. 5, bottom). These secondary bands were strongly red tinted and possessed a much longer wavelength and greater uniformity than the primary banding (Fig. 5). Following the convention of Abrajevitch *et al.* (2014), these bands will henceforth be referred to as the '*uniform*' pattern, with the regular, primary banding to be referred to as either the '*primary*' or '*newsprint*' pattern.

The primary 'newsprint' patterns at the Wittenoom outcrop exhibited regular increases in bandwidth and interband spacing parallel to the bedding direction (e.g., Fig. 7, top), consistent with the spacing and width laws characteristic of Liesegang banding. Spatial analysis of the pattern within a print stone sample from Wittenoom revealed a spacing coefficient of $p = 0.018 \pm 0.005$, as per equation 4.1. The width and spacing of each individual band are presented in Fig. 7.

https://doi.org/10.1180/mgm.2025.11 Published online by Cambridge University Press

4.2. Mineralogy

The composition of the print stone iron-oxide pigment was examined using XRD, with representative Rietveld refinements for the primary bands of each outcrop provided in Fig. 8, and relative mineral abundances presented in Fig. 9. In all samples, iron-oxide was predominately present as 5-10 μm grains of hematite and goethite, with each grain possessing a distinct cuboid morphology (Fig. 10 A & B). As hematite and goethite grains could not be distinguished under the SEM, any morphological differences between the two phases could not be determined. Smaller quantities of dissolution voids were likewise present throughout the dark and light banding (Fig. 10 A), with some voids also appearing cuboid (Fig. 10 C). These voids did not appear to be preferentially distributed within either the dark or light banding (Fig. 11).

Excluding the iron-bearing pigment, the mineralogical composition of print stone did not show any significant variation between the dark and light banding for a given outcrop. However, substantial differences were evident in the major (> 5 wt%) mineral phases between outcrops, varying from highly feldspathic assemblages (orthoclase + quartz ± muscovite ± kaolinite) at Wittenoom and Great Northern Highway to an alunite-dominated assemblage (alunite + quartz + muscovite) at Hamersley Ridge (Fig. 9). In both instances, the iron-oxide phases appeared to be texturally early with respect to the aluminosilicate mineral phases, including kaolinite and alunite. Further mineralogical differences were observed in print stone samples from Great Northern Highway, where 0.2-1 mm long needle-shaped crystals of ilmenite were disseminated throughout the light and dark banding, bisected in places by crosscutting calcite veins (Fig. 12).

The composition of the uniform banding of Hamersley Ridge print stone was also analysed by XRD, showing a moderate abundance of goethite (~5 wt%) and a near absence of hematite (~0.1 wt%). All other mineral phases within the uniform banding were unchanged relative to the mineralogical composition of the light banding.

4.3. Geochemistry

XFM and LA-ICP-MS analyses were used to identify heterogeneous trace element distributions between the light and dark banding of print stone. In comparison to eight typical post-Archean Australian shales (Taylor and McLennan, 1985), print stone exhibited consistent depletion of many trace metals, including Co, V, Cr, Ni, Sr, Y, Zr, Nb, Hf and Th (Fig. 13), with only Cu showing slight enrichment. No consistent differences between the dark and light banding were observed outside of Mo.

https://doi.org/10.1180/mgm.2025.11 Published online by Cambridge University Press

The distributions of REEs between Hamersley Ridge and Great Northern Highway are compared in Fig. 14. REE abundances in print stone are consistently well below the Post Archean Australian Shale (PAAS) values reported by Taylor and McLennan (1985). Positive Eu anomalies are present in both outcrops, while a strong enrichment of light REE relative to mid- and heavy-REE is observed at Hamersley Ridge. At Hamersley Ridge, the uniform and light banding shared a consistent REE distribution within uncertainties, while the dark, 'newsprint' pigment exhibited a significantly higher Eu anomaly, with further enrichment of middle REEs from Sm to Ho when compared to the white and uniform bandings. Relative to the white banding, a similar enhancement of the Eu anomaly is also observed in the dark banding of Rock Cutting print stone, alongside a general deletion of Er, Tm, Yb and Lu.

5. Discussion

5.1. Pattern morphology is consistent with Liesegang banding

Although both print stone and zebra rock are defined by series of regular, repeating bands that can rarely also manifest as spot- or rod-like morphologies (Figs. 3 & 5), the pattern of print stone is immediately distinguishable from that of zebra rock by its typically lower abundance of iron oxides, decreased band order and regularity, a much higher occurrence of band discontinuities and forking, and the extension of banding vertically into adjacent strata. Unlike zebra rock, print stone also exhibits the influence of intercutting joints upon pattern morphology (Fig. 5), indicating that print stone pattern development was not a near-surface, pedogenic process but rather developed well after lithification.

Strong evidence of the Liesegang phenomenon was observed in Wittenoom print stone samples where the banding was orientated perpendicular to the plane of bedding. In these samples, the band width and spacing coefficient increase with increasing distance from the pattern core, in a manner consistent with the Liesegang spacing and width laws (Fig. 7). The spacing coefficient in Wittenoom print stone is 0.018 ± 0.005 (Fig. 7), lower than the three non-zero spacing coefficients measured in zebra rock samples (0.054-0.071; Liu *et al.*, 2023), but within the general range established by laboratory experiments and computational modelling (0 - 0.5; e.g., Antal *et al.*, 1998; Thomas *et al.*, 2011; Yatsuda *et al.*, 2023). The initial conditions which define the spacing coefficient in Liesegang banding are not yet fully understood, but low diffusion coefficient ratios of the inner to outer reactants, high reactant concentrations and a low degree of super-saturation have all been determined to lower the spacing coefficient (Büki *et al.*, 1995). The spacing coefficient of Wittenoom print stone banding orientated parallel to bedding (that is, extending vertically up and down the

https://doi.org/10.1180/mgm.2025.11 Published online by Cambridge University Press

formation) could not be quantified due to complex changes to band morphology likely induced by variations in host rock permeability (e.g., Fig. 5).

5.2. Mineralogical evolution in print stone

The pigment of the primary print stone banding is composed entirely of variable quantities of hematite and goethite, with all other mineral phases appearing approximately homogeneous between the dark and light banding. By contrast, the uniform banding found in Hamersley Ridge print stone is almost exclusively composed of low to moderate quantities of goethite, as also reported by Abrajevitch *et al.* (2014). The distinct 5–10 μm cuboid morphology of hematite and goethite in the primary pattern (Fig. 10) strongly suggests that print stone banding was originally emplaced as pyrite.

Although absent in the studied print stone samples, pyrite is abundant within the Mount McRae Shale in two contrasting modes: large, polycrystalline pyrite nodules up to 10 cm in size, and disseminated, euhedral pyrite ranging from 10 to 20 μm in size (Haruna *et al.*, 2003; Slotznick *et al.*, 2022). No evidence of past or present nodular pyrite, thought to be syn-depositional in origin (Slotznick *et al.*, 2022), is observed in print stone. By contrast, micrometre-scale, euhedral pyrite within the Mount McRae Shale is considered to be hydrothermal on the basis of textural-relationships and extensive Mo- and As enrichments (Slotznick *et al.*, 2022). This disseminated pyrite is directly comparable in morphology, grain size, and Mo-enrichment, to the pseudomorphic hematite in print stone (Fig. 13), suggesting similar hydrothermal origins. Constraining the precise age and conditions of pyrite emplacement is difficult to ascertain due both to the absence of preserved pyrite in print stone and the pervasive hydrothermal activity within the Hamersley Group during the early Paleoproterozoic (e.g., Haruna *et al.*, 2003; Slotznick *et al.*, 2022; Rasmussen *et al.*, 2007). Hydrothermal pyrite in veins elsewhere in the Mount McRae Shale have been dated to 1.66, 2.05 and 2.20 Ga (U-Pb isotope dating; Slotznick *et al.*, 2022). The temperature and pH during original hydrothermal alteration are likewise difficult to quantify. However, the presence of hydrothermal crocidolite (~150,000 tons of this fibrous variety of riebeckite, $Na_2Fe^{2+}{}_3Fe^{3+}{}_2Si_8O_{22}(OH)_2$, were mined between 1937-1966; Western Australian Government, 2006) underlying the print stone deposit at Wittenoom suggests exposure of that section of the McRae Shale to large quantities of moderately hot hydrothermal fluids (T ~130˚C), with possible pH values ranging from near-neutral (pH 6.5) to moderately alkaline (Miyano and Klein, 1983). Given the frequent association of euhedral pyrite with crocidolite (Miyano and Klein, 1983) and the close geographical proximity of print stone and crocidolite

https://doi.org/10.1180/mgm.2025.11 Published online by Cambridge University Press

deposits at Wittenoom, it is considered likely that crocidolite and patterned pyrite were emplaced concurrently during the same hydrothermal event.

Replacement of the pyrite by hematite likely occurred much later, during the exposure of the patterned bedding to oxidising conditions. This oxidation most likely took place either in the Late Carboniferous (~325-310 Ma) or in the Mesoproterozoic (~1.5 Ga), based on the iron-oxide paleopole data from Abrajevitch *et al.* (2014). The kaolinite and alunite phases possibly also formed during this period, arising from the acidic alteration of host-rock orthoclase by sulfuric acid, an expected by-product of pyrite oxidation. The identification of carbonates (e.g., siderite, dolomite, calcite and ankerite) and extant pyrite elsewhere in the McRae Shale (Trendall and Blockley, 1970; Raiswell *et al.*, 2011), as well as the apparent absence of alunite and kaolinite in those same lithologies, suggests that the oxidation of pyrite and the associated acidic alteration of orthoclase was not pervasive throughout the entire formation.

The formation of the secondary, goethite-rich, 'uniform' banding overprinting the pattern at Hamersley Ridge has been ascribed a much later date of 15 – 25 Ma and is considered a result of goethite precipitation due to surface weathering (Abrajevitch *et al.*, 2014). As such, the development of the secondary banding can be considered unrelated to the emplacement of the primary 'newsprint' pattern.

5.3. Geochemical evidence for hydrothermal origin of pattern

The enhancement of the positive Eu anomaly in the dark bands of primary print stone patterns suggests that the emplacement of the iron-bearing pigment arose during a period of high Eu mobility, attributed to the predominance of Eu^{2+} over the less-soluble Eu^{3+}. At room temperature, Eu^{2+} is unstable in aqueous solution; however, the stability of Eu^{2+} relative to Eu^{3+} increases with increasing temperature, and Eu^{2+} becomes dominant under mildly reducing conditions (sulfate/bisulfide coexistence) above ~200˚C (Liu *et al.*, 2017). The reduction of Eu^{3+} to Eu^{2+} under reducing conditions at elevated temperatures can explain the increase in the strength of the Eu anomaly. For this reason, a positive Eu anomaly is often interpreted as an indicator of a hydrothermal component, and is demonstrated for example by the strong positive Eu anomaly found in many modern hydrothermal vent fluids (e.g., Michard and Albarede, 1986; Campbell *et al.*, 1988; Hinkley and Tatsumoto, 2012). However, it is also possible that positive Eu anomalies were derived from sedimentation in Archean oceans, which may have been Eu-enriched due to low oxygen levels preventing the scavenging of vent-emitted Eu by co-precipitation with Fe oxyhydroxides (Olivarez and

Owen, 1991; Sugahara *et al.*, 2010). As such, while the Eu geochemistry of print stone is consistent with a hydrothermal origin, this cannot be considered diagnostic on its own.

Unlike in the primary banding, no changes in the magnitude of the Eu anomaly are detected between the goethite-rich uniform banding and the adjacent light banding of Hamersley Ridge print stone (Fig. 14, top). Indeed, the REE contents of the uniform banding remained largely unchanged in comparison to the light banding, with the exception of minor enrichment of La, Ce, and Pr. The absence of relative Eu enrichment suggests that the uniform bands in Hamersley Ridge print stone were most likely not emplaced during the same period as the primary bands and are probably not hydrothermal in origin.

Trace elements are significantly depleted relative to PAAS, with lower average abundances of most heavy metals and all REEs (Figs. 13 & 14). A notable exception to this is Rb, which exhibits abundances on par with other Australian shales (Taylor and McLennan, 1985) and over an order of magnitude higher than in zebra rock (Coward *et al.*, 2023). Also of note is the substantial depletion of Sr when compared to both zebra rock and other Australian shales, implying the absence of svanbergite and other Sr-bearing aluminium-phosphate-sulfate (APS) minerals. A low Rb/Sr ratio, like that observed in zebra rock (0.003–0.04; (Coward *et al.*, 2023), is typically indicative of advanced argillic alteration due to acidic leaching of Rb, as well as the fixing of Sr within APS minerals (Hikov, 2004; Hikov *et al.*, 2017). By contrast, the Rb/Sr ratio of print stone ranges from 2–28, suggesting that these outcrops lacked the high acidity necessary to leach Rb, as well as the oxidising conditions normally required for the precipitation of APS phases.

5.4. Comparison to zebra rock

Print stone shares many morphological and mineralogical similarities with Ediacaran-age zebra rock from the East Kimberley region of Western Australia, raising the possibility that both patterned siltstones may have developed through related mechanisms. Indeed, the formation of zebra rock through hydrothermally induced Liesegang banding has been proposed by several recent studies (Loughnan and Roberts, 1990; Kawahara *et al.*, 2022; Coward *et al.*, 2023; Yatsuda *et al.*, 2023).

Unlike other examples of iron-oxide banding, zebra rock and print stone patterns are both well-defined and highly ordered, with sharp band edges, a similar spacing coefficient, and a wide variation of pattern morphologies, including spots and rods. Alongside their morphological similarities, print stone and zebra rock also possess many of the same mineral phases, most notably hematite, alunite, kaolinite, and muscovite (Loughnan and Roberts,

https://doi.org/10.1180/mgm.2025.11 Published online by Cambridge University Press

1990; Kawahara *et al.*, 2022; Coward *et al.*, 2023). The presence of alunite and kaolinite in print stone and zebra rock suggest that both patterned siltstones were likely exposed to acid-sulfate solutions. However, the absence of feldspar in zebra rock, alongside the increased abundance of hematite, alunite, kaolinite, and APS minerals, and a much lower Rb/Sr ratio (Coward *et al.*, 2023), suggests that zebra rock experienced more oxidising and acidic conditions during this period relative to print stone.

Perhaps the greatest difference between the two banded siltstones is the morphology of the iron-oxide pigment within the dark banding. In zebra rock, the pigment is composed of texturally-late aggregates of 0.2 – 1 μm hexagonal hematite platelets, distributed within the interstitial spacing between larger quartz, kaolinite, and alunite grains. In print stone, the pigment is instead composed of 5 – 10 μm cubic grains of texturally early, pseudomorphic hematite and goethite. The significant differences between the grain-size, morphology, and textural relationships of the iron-oxide phase of both rocks suggests that while the underlying mechanism of self-organisation may be similar, the banding of print stone and zebra rock likely developed under dissimilar geochemical conditions.

5.5. Pattern formation

The changes in pattern morphology around intercutting joints (Fig. 5) and the deposition of iron-oxides along bedding planes (Fig. 6) strongly suggest that print stone banding occurred during iron-rich fluid infiltration through joint and pore networks. The formation of banding during this process was likely the result of the Liesegang phenomenon, as evidenced by the adherence of the pattern to Liesegang spacing laws when constrained within relatively homogenous bedding (Fig. 7).

The probable pyritic origin of the hematite pigment, in conjunction with its strong, positive Eu anomaly and the close association with hydrothermal crocidolite at Wittenoom, suggest that the precursor pyrite phase was deposited by strongly reducing, slightly acidic to alkaline, sulfide-bearing hydrothermal fluids (T~130˚C) during the Early Paleoproterozoic. Later, during the Mesoproterozoic or the Late Carboniferous, erosion of overlying formations facilitated the oxidation and replacement of pyrite by pseudomorphic hematite and goethite, which in turn likely initiated the partial acidic alteration of orthoclase to produce kaolinite and alunite. The development of Liesegang bands in print stone likely occurred during one of these two time periods, i.e., during pyrite formation in the Early Paleoproterozoic, or during pyrite oxidation in the Mesoproterozoic/Late Carboniferous.

https://doi.org/10.1180/mgm.2025.11 Published online by Cambridge University Press

Of the two alternatives, a Mesoproterozoic/Late Carboniferous formation is considered the least compelling. In this instance, self-organisation of the iron-bearing phase would have been initiated by the oxidation of uniformly distributed pyrite, producing an acidic and possibly ferric solution. As this fluid diffuses through the formation, it may react with, and be neutralised by, carbonate-rich sediments, as found elsewhere in Mount McRae Shale (e.g., Raiswell *et al.*, 2011). In this case, neutralisation of the acidic fluids by carbonate dissolution induces the precipitation of dissolved ferric iron (which is relatively insoluble at pH >3) into available pore spaces (including pyritic dissolution voids) as iron-oxides or oxyhydroxides. Similar mechanisms have been proposed for the formation of hematite Liesegang banding in other sediments, including zebra rock (Kawahara *et al.*, 2022; Coward *et al.*, 2023). However, despite similarities to current theories regarding pattern formation in zebra rock, this hypothesis is considered less likely due to two observations. Firstly, the iron-oxides in print-stone appear texturally early with respect to alunite and kaolinite (which most likely formed from silicate-acid sulfate interactions arising as a direct by-product of pyrite oxidation) and are not observed within the interstitial spacing between alunite, kaolinite, and quartz grains (Fig. 10A), unlike in zebra rock (Coward *et al.*, 2023). This relationship is not consistent with the extensive mobilisation, diffusion, and reprecipitation of iron required to form Liesegang banding through the oxidation and dissolution of pyrite. Secondly, while semi-cubic dissolution voids were observed in print stone (Fig. 10C), these did not appear to be preferentially distributed within the light banding, which would be expected to occur if the majority of dissolution voids within the dark banding had been infilled by iron-oxide precipitates. Rather, however, pyritic dissolution voids were observed to be distributed uniformly throughout both the dark and light banding (Fig. 11). Furthermore, the dissolution voids in both the light and dark banding appear to be on average smaller and less prevalent than the pseudomorphic iron-oxides (Fig. 10 & 11), suggesting an origin unrelated to the pattern-forming pyrite phase.

The second alternative is that self-organisation in print stone arose during the original deposition of hydrothermal pyrite in the Early Proterozoic. The periodic deposition of pyrite into banding has been previously recognised in sapropelic sediments in the Eastern Mediterranean by Passier *et al.* (1996). Subsequent modelling by Bektursunova and L'Heureux (2011) identified this banding as likely resulting from the Liesegang mechanism, finding that the counter-diffusion of ferrous iron and hydrogen sulfides resulted in pyritic banding resembling Liesegang patterns. Note that this mechanism can happen up to high temperatures, e.g. in skarn deposits at contact metamorphic conditions (e.g., Ciobanu and

https://doi.org/10.1180/mgm.2025.11 Published online by Cambridge University Press

Cook, 2004). We hypothesise that a similar reaction (at higher temperatures) may have arisen in the Mount McRae Shale through the infiltration of a reducing, sulfidic hydrothermal fluid into sediments bearing uniformly distributed Fe(II) mineral phases such as siderite, which is prevalent throughout the formation in the form of sideritic BIFs (Raiswell *et al.*, 2011). Counter-diffusion of the ferrous iron and sulfide rich solutions could have resulted in pyritic Liesegang bands, with later oxidation occurring without significant iron mobilisation and resulting in the direct replacement of banded pyrite by pseudomorphic hematite and goethite.

6. Conclusions

This study reached several conclusions regarding pattern development in Pilbara print stone, as summarised below:

1. As evidenced by general band morphology and adherence of the pattern to the spacing law, periodic self-organisation in print stone likely arose due to the occurrence of the Liesegang phenomenon.
2. A strong, positive Eu anomaly and distinct cuboid morphology of the iron-oxide pigment, alongside evidence of iron deposition along fluid transport pathways, suggest that print stone Liesegang banding was initiated by the infiltration of a sulfidic, near-neutral hydrothermal fluid into ferrous, feldspathic sediment, resulting in periodic pyrite precipitation. This pyrite was later oxidised, forming pseudomorphic hematite and goethite. This hypothesis is further supported by the presence of hydrothermal pyrite elsewhere in the McRae Shale, and extensive hydrothermal crocidolite underlying print stone beds at Wittenoom. An alternative hypothesis, that Liesegang banding was instead initiated during pyrite oxidation, was also considered. However, this mechanism is considered unlikely due to both the early precipitation of the iron-oxide phase relative to kaolinite and alunite, and inconsistencies in the size, abundance, and expected distribution of observed cuboid-dissolution voids relative to the pseudomorphic iron-oxide phase.
3. Pattern formation in print stone occurred in early Paleoproterozoic, at a time of extensive hydrothermal activity in the Mount McRae Shale. The oxidation of pyrite and replacement by hematite occurred later, either in the Mesoproterozoic or Late Carboniferous. Pyrite oxidation produced acidic, sulfate-rich fluids, that are responsible for the partial alteration of detrital orthoclase, leading to the formation of alunite and kaolinite.
4. The close morphological and mineralogical similarities between print stone and East Kimberley zebra rock provides further support to the hypothesis that zebra rock may

https://doi.org/10.1180/mgm.2025.11 Published online by Cambridge University Press

have also formed via the process of hydrothermally mediated Liesegang banding. However, the positive Eu anomaly, high Rb/Sr ratio, and distinctive cuboid morphology of the iron-oxide phase suggests that these hydrothermal fluids were likely less acidic and more reducing than those responsible of pattern formation in zebra rock.

Acknowledgments

We acknowledge the use of instruments and scientific and technical assistance at the Monash Centre for Electron Microscopy (MCEM) at Monash University, the Environmental Economic Geology Laboratory at the University of Alberta, the Victorian Node of Microscopy Australia, and the use of facilities within the Monash X-ray Platform. Parts of this research were also undertaken on the XFM and Imaging and Medical beamlines at the Australian Synchrotron, part of the Australian Nuclear Science and Technology Organisation (ANSTO). We thank Dr. Helen Brand and Dr. David Paterson for technical help and expertise provided at the Australian Synchrotron, Baolin Wang for his assistance in obtaining XRD patterns at the University of Alberta. We acknowledge financial support from an Australian Government Research Training Program (RTP) Scholarship (A.C.). The paper benefited from insightful comments from Huan Li (Central South University, China) and an anonymous reviewer.

Competing Interests

The author(s) declare none.

References

Abrajevitch, A., Pillans, B.J. and Roberts, A.P. (2014) Haematite pigmentation events and palaeomagnetic recording: Implications from the Pilbara print stone, western Australia. *Geophysical Journal International*, 199, 658-672.

Abrajevitch, A., Pillans, B.J., Roberts, A.P. and Kodama, K. (2018) Magnetic properties and paleomagnetism of zebra rock, Western Australia: Chemical remanence acquisition in hematite pigment and Ediacaran geomagnetic field behavior. *Geochemistry, Geophysics, Geosystems*, 19, 732-748.

Abramoff, M.D., Magalhaes, P.J., Ram, S.J. (2004) Image Processing with ImageJ. *Biophotonics International*, 11, 36-42

https://doi.org/10.1180/mgm.2025.11 Published online by Cambridge University Press

Anbar, A.D., Duan, Y., Lyons, T.W., Arnold, G.L., Kendall, B., Creaser, R.A., Kaufman, A.J., Gordon, G.W., Scott, C., Garvin, J. and Buick, R. (2007) A whiff of oxygen before the great oxidation event? *Science*, 317, 1903-1907

Antal, T., Droz, M. Magnin, J., Racz, Z. and Zrinyi, M.. (1998) Derivation of the Matalon-Packter law for Liesegang patterns. *Journal of Chemical Physics*, 109, 9479-9486

Bektursunova, R. and L'Heureux, I. (2011) A reaction-transport model of periodic precipitation of pyrite in anoxic marine sediments. *Chemical Geology*, 287, 158-170.

Büki A., Kárpáti-Smidróczki É., Zrínyi M. (1995) Computer simulation of regular Liesegang structures. *Journal of Chemical Physics*, 103, 10387-10392.

Campbell, A.C., Bowers, T.S., Measures, C.I., Falkner, K.K., Khadem, M. and Edmond, J.M. (1988) A time series of vent fluid compositions from 21°N, East Pacific Rise (1979, 1981, 1985) and the Guaymas basin, gulf of California (1982, 1985). *Journal Geophysical Research*, 93, 4537-4550.

Ciobanu, C.L., Cook, N.J., 2004. Skarn textures and a case study: the Ocna de Fier-Dognecea orefield, Banat, Romania. *Ore Geology Reviews* 24, 315-370.

Coelho AA, Evans JSO, Evans IR, Kern A, Parsons S (2011) The TOPAS symbolic computation system. *Powder Diffraction*, 26:S22-S25. doi:10.1154/1.3661087

Coward, A.J., Slim, A.C., Brugger, J., Wilson, S., Williams, T., Pillans, B. and Maksimenko, A. (2023) Mineralogy and geochemistry of pattern formation in zebra rock from the East Kimberley, Australia. *Chemical Geology*, 622.

Droz, M., Magnin, J. and Zrinyi, M. (1999) Liesegang patterns: Studies on the width law. *The Journal of Chemical Physics*, 110, 9618-9622.

Hartman, R.J. and Dickey, R.M. (1932) The Liesegang phenomenon applied to the Lake Superior iron formations. *Journal of Physical Chemistry*, 36, 1129−1135.

Haruna, M., Hanamuro, T., Uyeda, K., Fujimaki, H. and Ohmoto, H. (2003) Chemical, isotopic, and fluid inclusion evidence for the hydrothermal alteration of the footwall rocks of the BIF-hosted iron ore deposits in the Hamersley district, Western Australia. *Resource Geology*, 53, 75-88.

Hikov, A. (2004) Geochemistry of strontium in advanced argillic alteration systems - possible guide to exploration. Pp. 29–31 in: *Bulgarian Geological Society, Annual Scientific Conference "Geology 2004", Abstracts*.

Hikov, A., Velinova, N., Catherine, L. and Kunov, A. (2017) Geochemistry of advanced argillic altered rocks in the area of Breznik, Western Srednogorie unit (Bulgaria). *Geologica Balcanica*, 46, 93–108.

https://doi.org/10.1180/mgm.2025.11 Published online by Cambridge University Press

Hinkley, T.K. and Tatsumoto, M. (2012) Metals and isotopes in Juan de Fuca Ridge hydrothermal fluids and their associated solid materials. *Journal of Geophysical Research: Solid Earth*, 92, 11400-11410.

Jablczynski, K. (1923) The rhythmic formation of precipitates. Liesegang rings. *Bulletin de la Société Chimique*, 33, 1592.

Kaufman, A.J., Johnston, D.T., Farquhar, J., Masterson, A.L., Lyons, T.W.B., S., Anbar, A.D., Arnold, G.L., Garvin, J. and Buick, R. (2007) Late Archean biospheric oxygenation and atmospheric evolution. *Science*, 317, 1900–1903.

Kawahara, H., Yoshida, H., Yamamoto, K., Katsuta, N., Nishimoto, S., Umemura, A. and Kuma, R. (2022) Hydrothermal formation of Fe-oxide bands in zebra rocks from northern Western Australia. *Chemical Geology*, 590.

Klein, C. (2005) Some Precambrian banded iron-formations (BIFs) from around the world: Their age, geologic setting, mineralogy, metamorphism, geochemistry, and origin. *American Mineralogist*, 90, 1473-1499.

Liu, W.H., Etschmann, B., Migdisov, A., Boukhalfa, H., Testemale, D., Muller, H., Hazemann, J.L. and Brugger, J. (2017) Revisiting the hydrothermal geochemistry of europium(II/III) in light of new *in-situ* XAS spectroscopy results. *Chemical Geology*, 459, 61-74.

Liu C, Calo VM, Regenauer-Lieb K, Hu M (2023) Coefficients of reaction-diffusion processes derived from patterns in rocks. *Journal of Geophysical Research: Solid Earth*, 128(5) doi:10.1029/2022jb026253

Loughnan, F.C. and Roberts, F.I. (1990) Composition and origin of the 'zebra rock' from the East Kimberley region of Western Australia. *Australian Journal of Earth Sciences*, 37, 201–205.

Michard, A. and Albarede, F. (1986) The REE content of some hydrothermal fluids. *Chemical Geology*, 55, 51-60.

Miyano, T. and Klein, C. (1983) Conditions of riebeckite formation in the iron-formation of the Dales Gorge member, Hamersley Group, Western-Australia. *American Mineralogist*, 68, 517-529.

Müller, S.C., Kai, S. and Ross, J. (1982) Curiosities in periodic precipitation patterns. *Science*, 216, 635-637.

Olivarez, A.M. and Owen, R.M. (1991) The europium anomaly of seawater: Implications for fluvial versus hydrothermal REE inputs to the oceans. *Chemical Geology*, 92, 317-328.

https://doi.org/10.1180/mgm.2025.11 Published online by Cambridge University Press

Passier, H.F., Middelburg, J.J., van Os, B.J.H. and de Lange, G.J. (1996) Diagenetic pyritisation under eastern Mediterranean sapropels caused by downward sulphide diffusion. *Geochimica et Cosmochimica Acta*, 60, 751-763.

Paulissen, W.E. and Luthi, S.M. (2011) High-frequency cyclicity in a Miocene sequence of the Vienna basin established from high-resolution logs and robust chronostratigraphic tuning. *Palaeogeography, Palaeoclimatology, Palaeoecology*, 307, 313-323.

Perugini, D., Little, M. and Poli, G. (2006) Time series to petrogenesis: Analysis of oscillatory zoning patterns in plagioclase crystals from lava flows. *Periodico Di Mineralogia*, 75, 263-276.

Raiswell, R., Reinhard, C.T., Derkowski, A., Owens, J., Bottrell, S.H., Anbar, A.D. and Lyons, T.W. (2011) Formation of syngenetic and early diagenetic iron minerals in the late Archean Mt. McRae Shale, Hamersley Basin, Australia: New insights on the patterns, controls and paleoenvironmental implications of authigenic mineral formation. *Geochimica et Cosmochimica Acta*, 75, 1072-1087.

Rasmussen, B., Blake, T.S. and Fletcher, I.R. (2005) U-Pb zircon age constraints on the Hamersley spherule beds: Evidence for a single 2.63 Ga Jeerinah-Carawine impact ejecta layer. *Geology*, 33, 725–728.

Rasmussen, B., Fletcher, I.R., Muhling, J.R., Thorne, W.S. and Broadbent, G.C. (2007) Prolonged history of episodic fluid flow in giant hematite ore bodies: Evidence from in situ U–Pb geochronology of hydrothermal xenotime. Earth and Planetary Science Letters, 258, 249-259.

Reinhard, C.T., Raiswell, R., Scott, C., Anbar, A.D. and Lyons, T.W. (2009) A Late Archean sulfidic sea stimulated by early oxidative weathering of the continents. *Science*, 326, 713-716.

Retallack, G.J. (2020) Zebra rock and other Ediacaran paleosols from western Australia. *Australian Journal of Earth Sciences*, 68, 532–556.

Shore, M. and Fowler, A.D. (1996) Oscillatory zoning in minerals: A common phenomenon. *Canadian Mineralogist*, 34, 1111-1126.

Slotznick, S.P., Johnson, J.E., Rasmussen, B., Raub, T.D., Webb, S.M., Zi, J.-W., Kirschvink, J.L. and Fischer, W.W. (2022) Reexamination of 2.5 Ga "whiff" of oxygen interval points to anoxic ocean before GOE. *Science Advances*, 8, eabj7190.

Sugahara, H., Sugitani, K., Mimura, K., Yamashita, F. and Yamamoto, K. (2010) A systematic rare-earth elements and yttrium study of Archean cherts at the Mount Goldsworthy greenstone belt in the Pilbara craton: Implications for the origin of microfossil-bearing black cherts. *Precambrian Research*, 177, 73-87.

https://doi.org/10.1180/mgm.2025.11 Published online by Cambridge University Press

Taylor, S.R. and McLennan, F.S. (1985) The continental crust: Its composition and evolution. Pp. 312. Blackwell Sci. Pub., Oxford.

Thorne, A.M. and Tyler, I.M. (1997) Roy Hill. 1:250000 geological series, explanatory notes. Geological Survey of Western Australia, Second Edition, 23 pp.

Thomas, S., Varghese, G., Lagzi, I. (2011) The width of Liesegang bands: A study using moving boundary model and simulation. *Pramana - Journal of Physics*, 78, 135-145

Trendall, A.F. and Blockley, J.G. (1970) The iron formations of the Precambrian Hamersley group, Western Australia, with special reference to the associated crocidolite. *Geological survey of Western Australia*, Bulletin 119, 366 pp.

Trendall, A.F., Compston, W., Nelson, D.R., De Laeter, J.R. and Bennett, V.C. (2004) Shrimp zircon ages constraining the depositional chronology of the Hamersley Group, Western Australia. *Australian Journal of Earth Sciences*, 51, 621-644.

Western Australian Government (2006). Management of asbestos contamination in Wittenoom (GHD-PB Report). Retrieved from https://www.wa.gov.au/system/files/2021-04/CL-GHD_PB_Report_Management_of_asbestos_contamination_in_Wittenoom.pdf

Yatsuda, Y., Tsushima, K., Fang, Q. and Nabika, H. (2023) Chemical model for pattern formation in rocks via periodic precipitation of iron oxide minerals. *ACS Earth and Space Chemistry*, 7, 2042-2049.

https://doi.org/10.1180/mgm.2025.11 Published online by Cambridge University Press

Figure captions

Figure 1*: Side and front view of a sample of print stone from near Wittenoom, compared to a sample of Zebra Rock from East Kimberley (Coward et al. 2023).*

https://doi.org/10.1180/mgm.2025.11 Published online by Cambridge University Press

***Figure 2**: Location of the three print stone outcrops examined in this study relative to the lithostratigraphy of the Mount McRae Shale and other associated formations. Map and geological data adapted from GeoVIEW.WA*

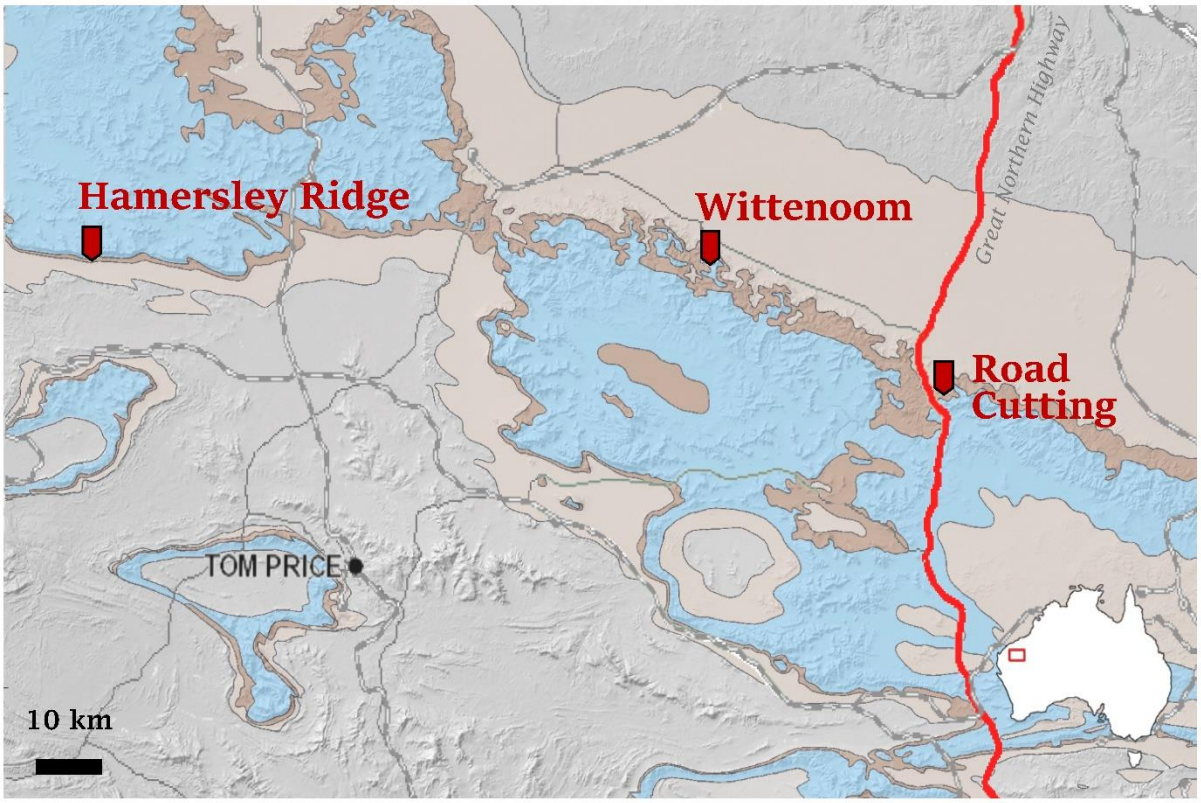

Brockman Iron Formation		2,470 Ma
Mt McRae Shale and Mount Sylvia Formations		~2,500 Ma
Wittenoom Formation		2,542–2,590 Ma
Undifferentiated formations		–

https://doi.org/10.1180/mgm.2025.11 Published online by Cambridge University Press

***Figure 3**: Print stone outcrops at Wittenoom (WT), Great Northern Highway (GNH) and Hamersley Ridge (HR).*

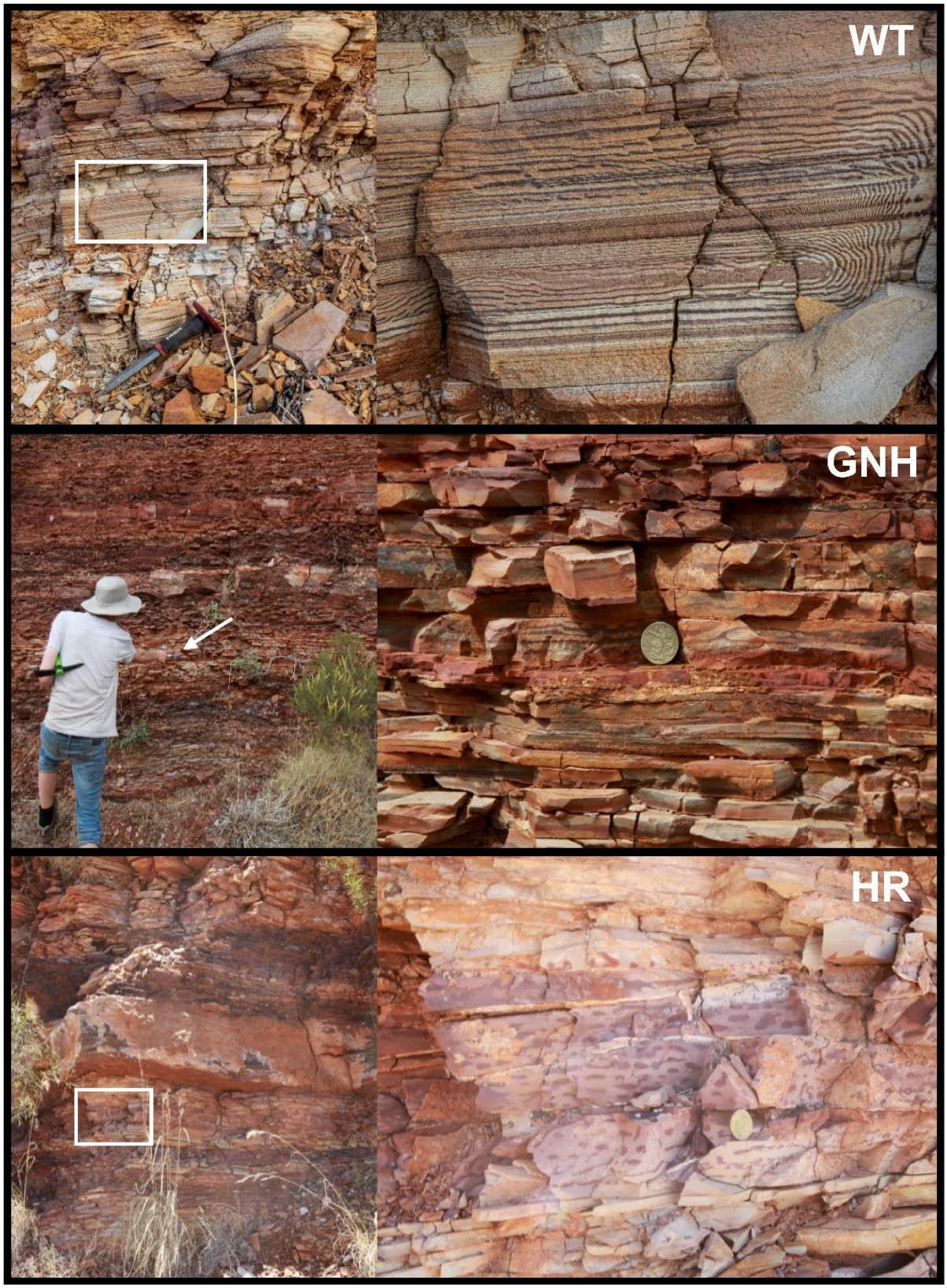

https://doi.org/10.1180/mgm.2025.11 Published online by Cambridge University Press

***Figure 4**: Two internal slices of the three-dimensional pattern morphology of print stone sample WT-02 from Wittenoom, as determined by X-ray tomography.*

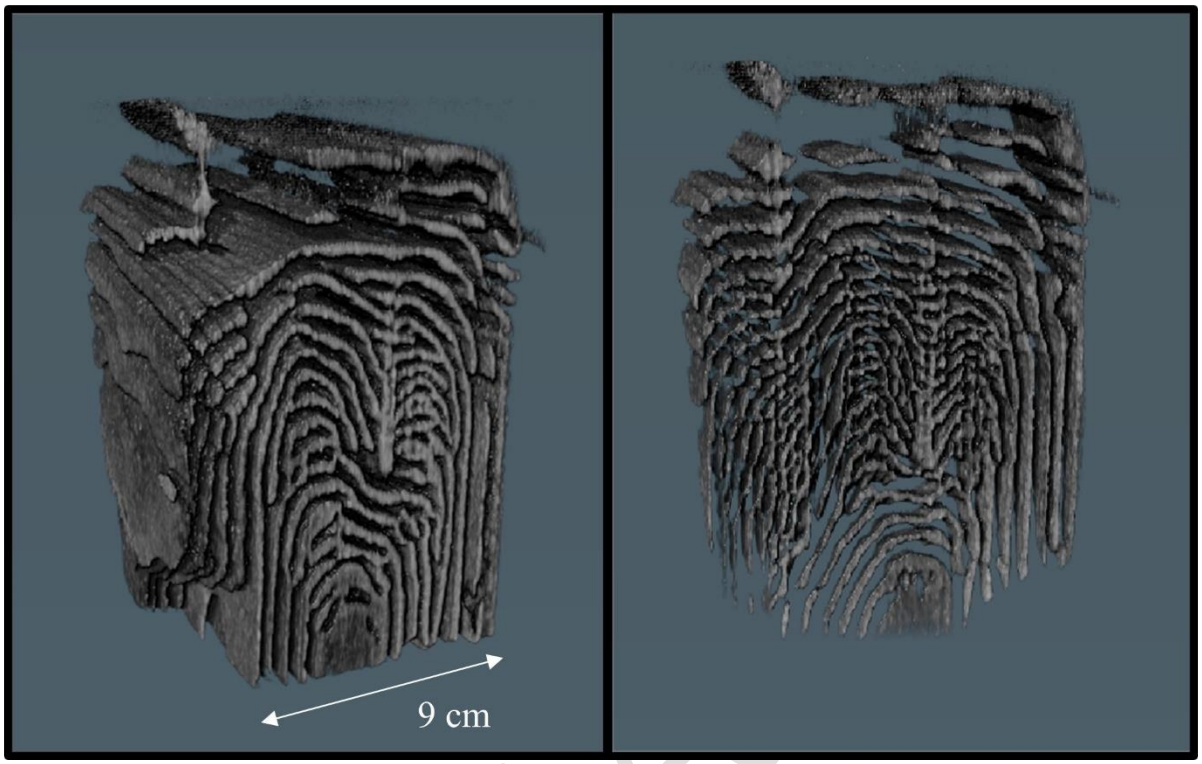

https://doi.org/10.1180/mgm.2025.11 Published online by Cambridge University Press

***Figure 5**: Images of in-situ print stone patterns at Wittenoom (top) and Hamersley Ridge (bottom). Of note are the changes in pattern wavelength across the vertical axis **(1)**, intercutting joints influencing pattern morphology **(2)**, and the diffuse secondary banding underlying the primary pattern **(3)**.*

https://doi.org/10.1180/mgm.2025.11 Published online by Cambridge University Press

***Figure 6**: X-ray fluorescence microscopy (XFM) M images of the distribution of Fe in print stone. (A): sample WT-4 from Wittenoom. (B): sample PS-L2-1 from Great Northern Highway.*

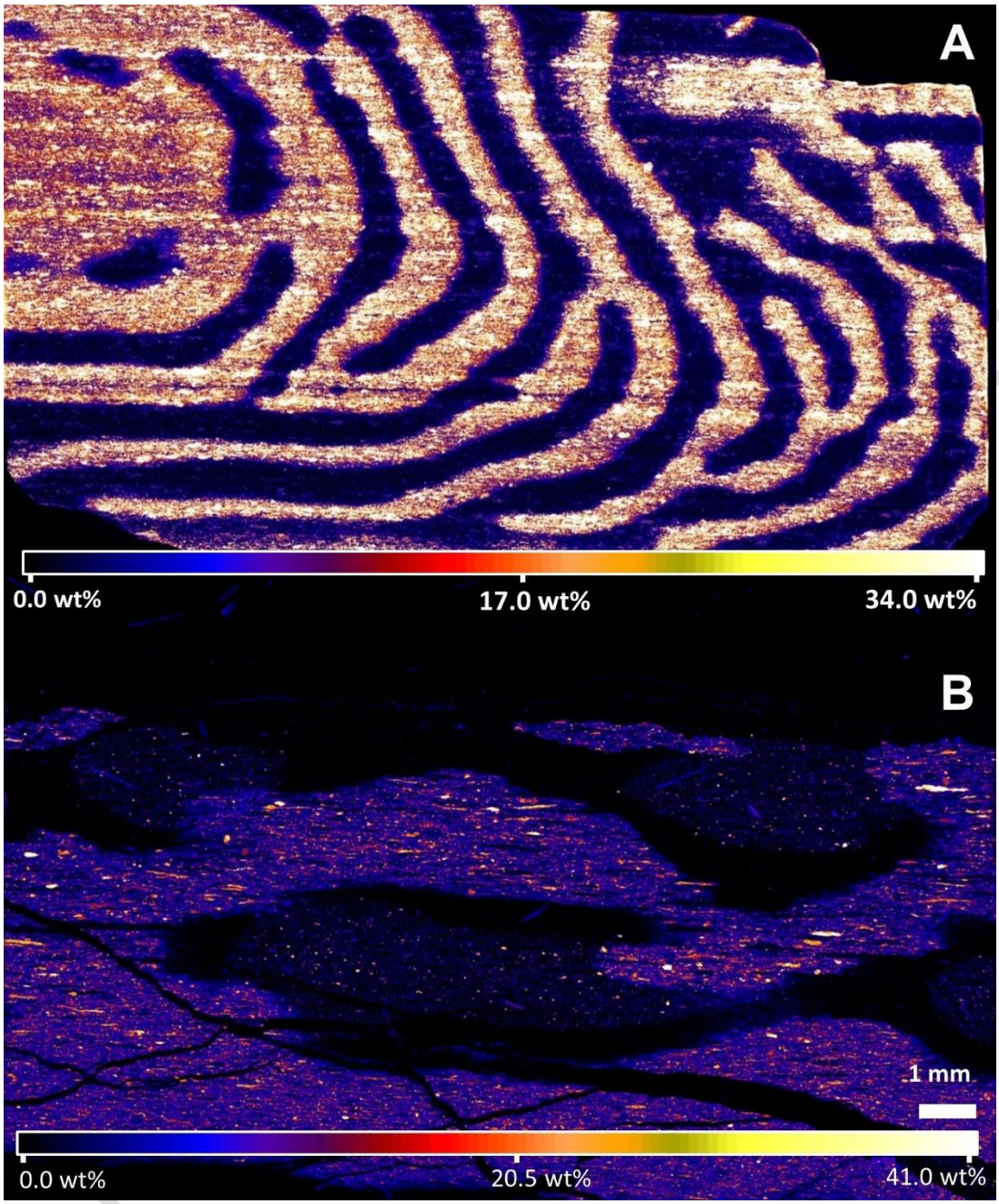

https://doi.org/10.1180/mgm.2025.11 Published online by Cambridge University Press

***Figure 7**: Spatial analysis data for print stone sample WT07. **Top**: sample WT07 after the application of colour thresholds to highlight band position. The line across which the spacing and width of the bands was determined has been marked with a red arrow. **Middle**: plot of the distance (X_{n+1}-X_n) between each band (X_n). **Bottom**: plot of the width (W_n) of each band (X_n).*

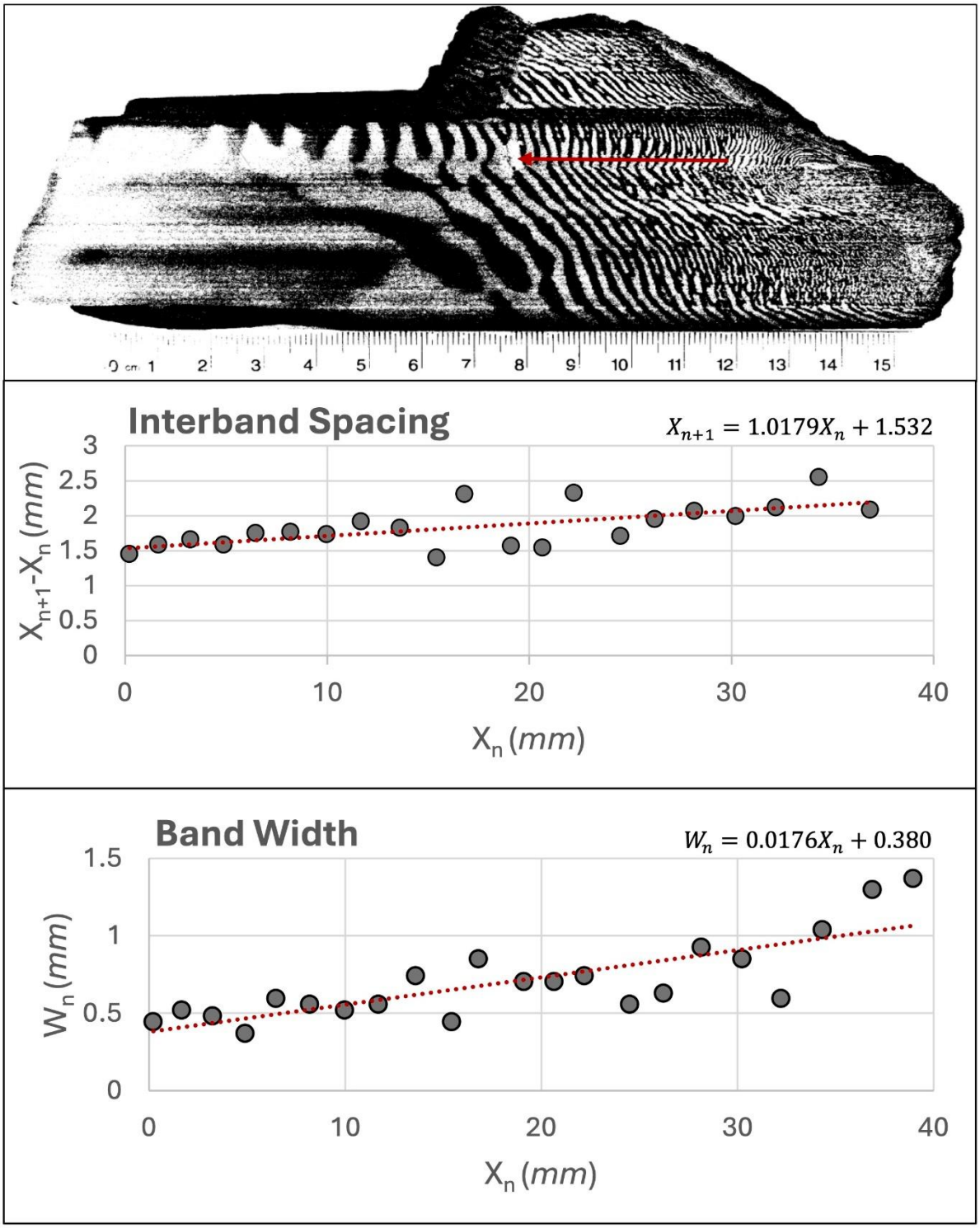

https://doi.org/10.1180/mgm.2025.11 Published online by Cambridge University Press

***Figure 8**: Representative Rietveld refinements from each of the three outcrops examined in this study. Concentration expressed as wt%.*

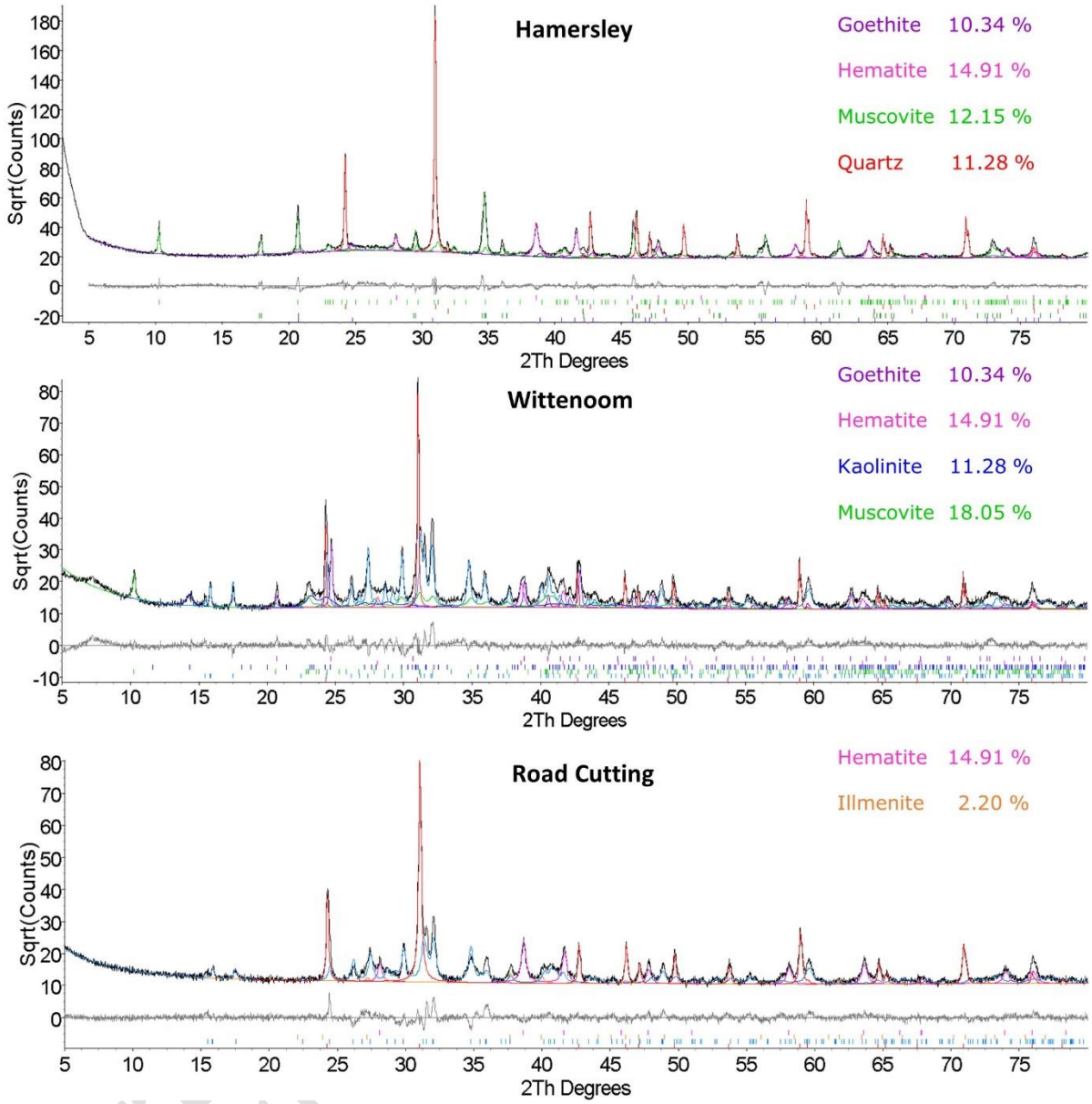

https://doi.org/10.1180/mgm.2025.11 Published online by Cambridge University Press

***Figure 9**: Abundances of mineral phases in the dark (**top**) and light (**bottom**) banding of print stone from each of the three examined outcrops, as determined by XRD Rietveld refinement. Mineralogy of the uniform bands in Hamersley Ridge are also included. Note that the calcite veins intercutting Great Northern Highway were not sampled for this analysis. Uncertainties derived from TOPAS* (Coelho *et al.*, 2011).

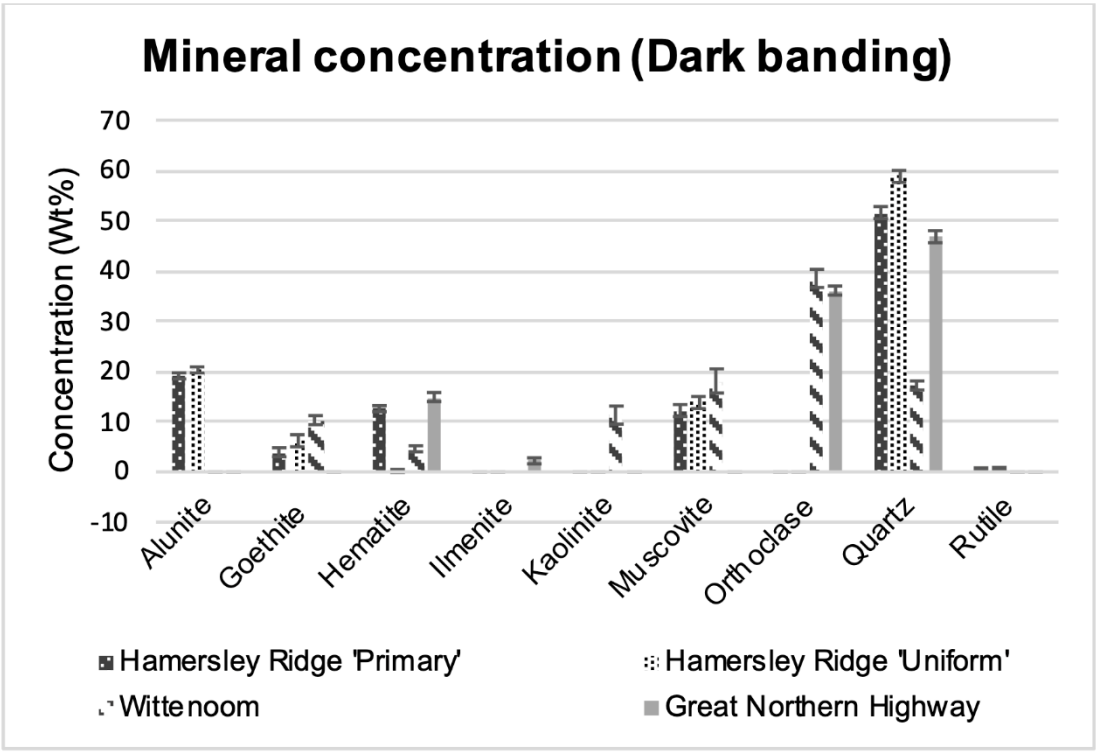

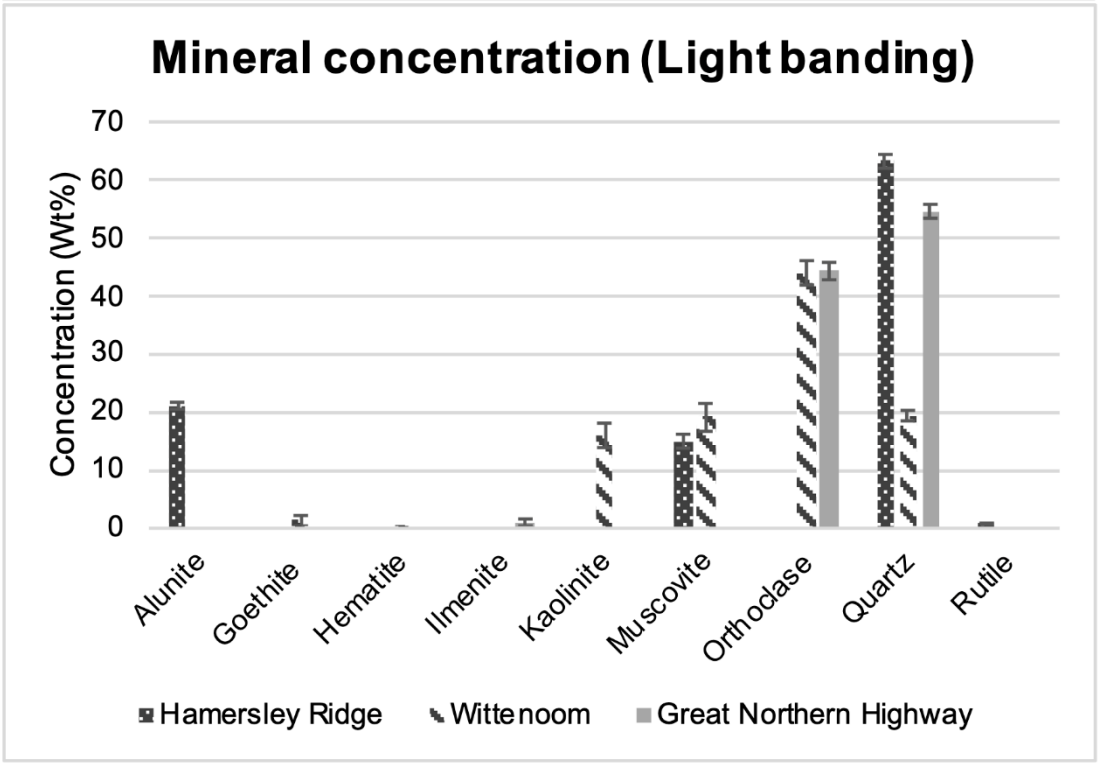

https://doi.org/10.1180/mgm.2025.11 Published online by Cambridge University Press

***Figure 10**: Distribution and morphology of iron-oxides and voids in print stone. **A:** Cuboid hematite grains and dissolution voids in the dark banding. **B:** Close-up of cuboid iron-oxide grain. **C:** Cuboid dissolution void in the light banding. All BSE images obtained by SEM from sample CW-2 from Hamersley Ridge deposit.*

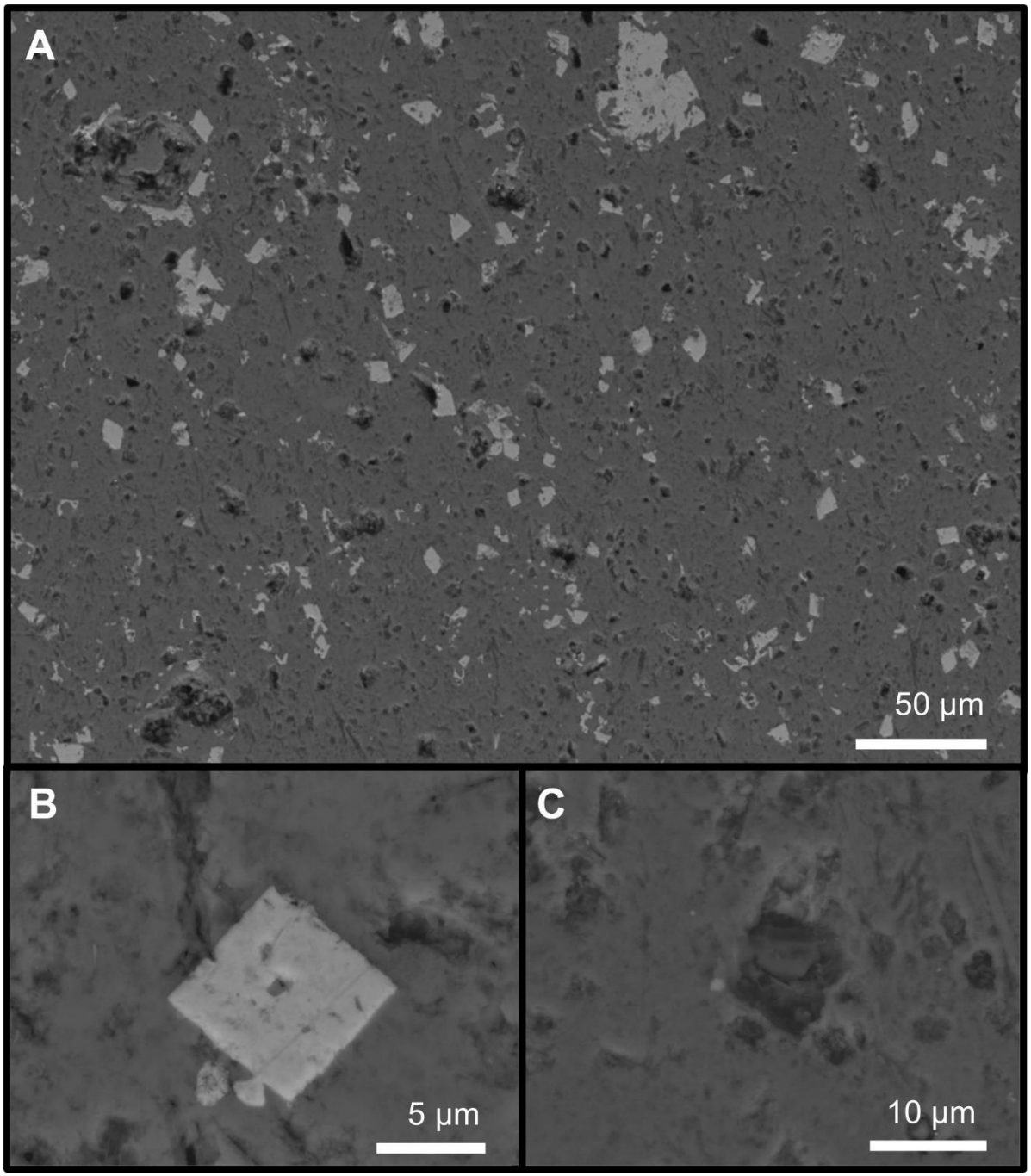

https://doi.org/10.1180/mgm.2025.11 Published online by Cambridge University Press

***Figure 11**: Interface between the dark (left) and light (right) banding of print stone, contrast-adjusted to highlight the heterogeneous distribution of iron-oxides (white) and the uniform distribution of dissolution voids (black). BSE image obtained by SEM from sample CW-2 from Hamersley Ridge deposit.*

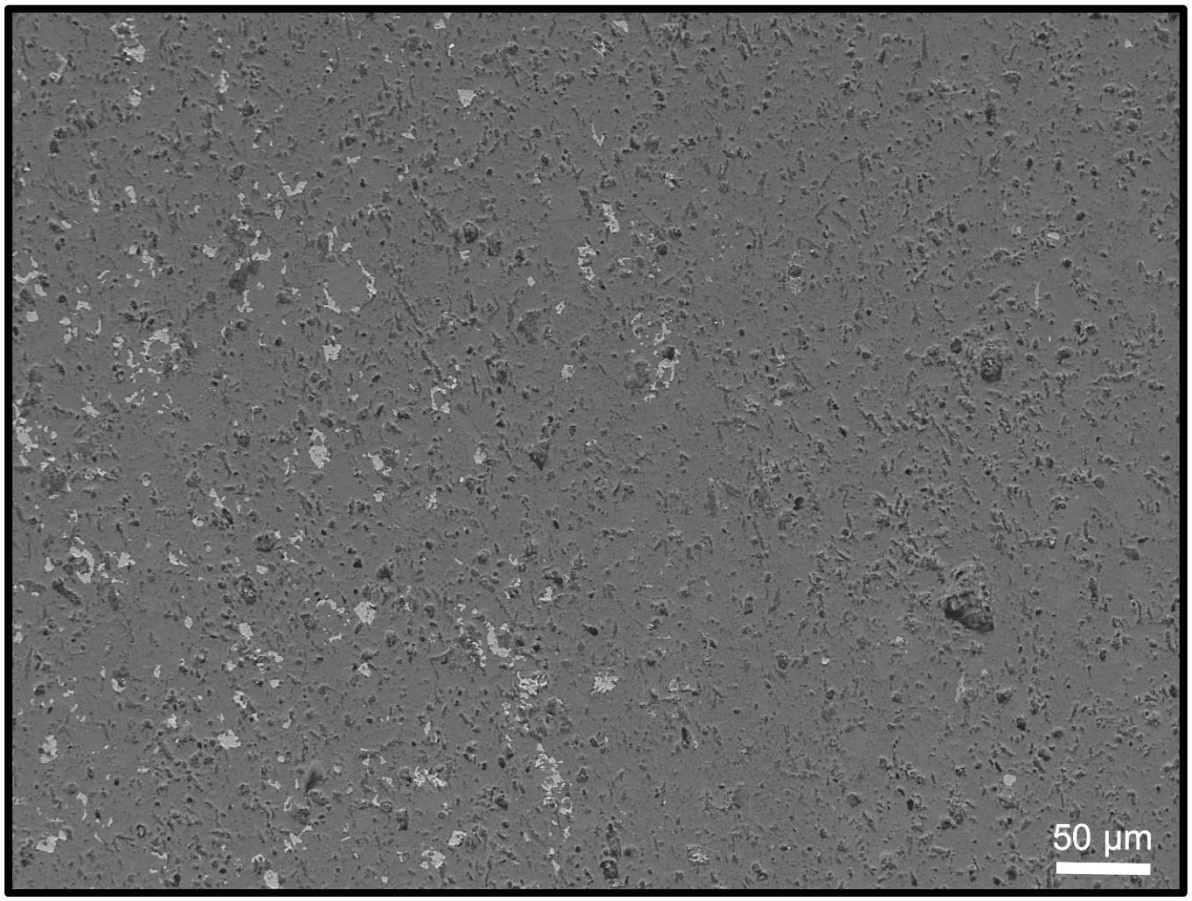

https://doi.org/10.1180/mgm.2025.11 Published online by Cambridge University Press

***Figure 12**: BSE (top) and EDS (bottom) composite image of Great Northern Highway print stone showing the distribution of Fe (red), Ti (yellow), Ca (orange), Si (dark blue), and Al (light blue). Highlighted in this image are intercutting calcite veins (Cal), large ilmenite crystals (Ilm) and hematite pigment (Hem), interspersed within a matrix of quartz (Qz) and orthoclase (Or).*

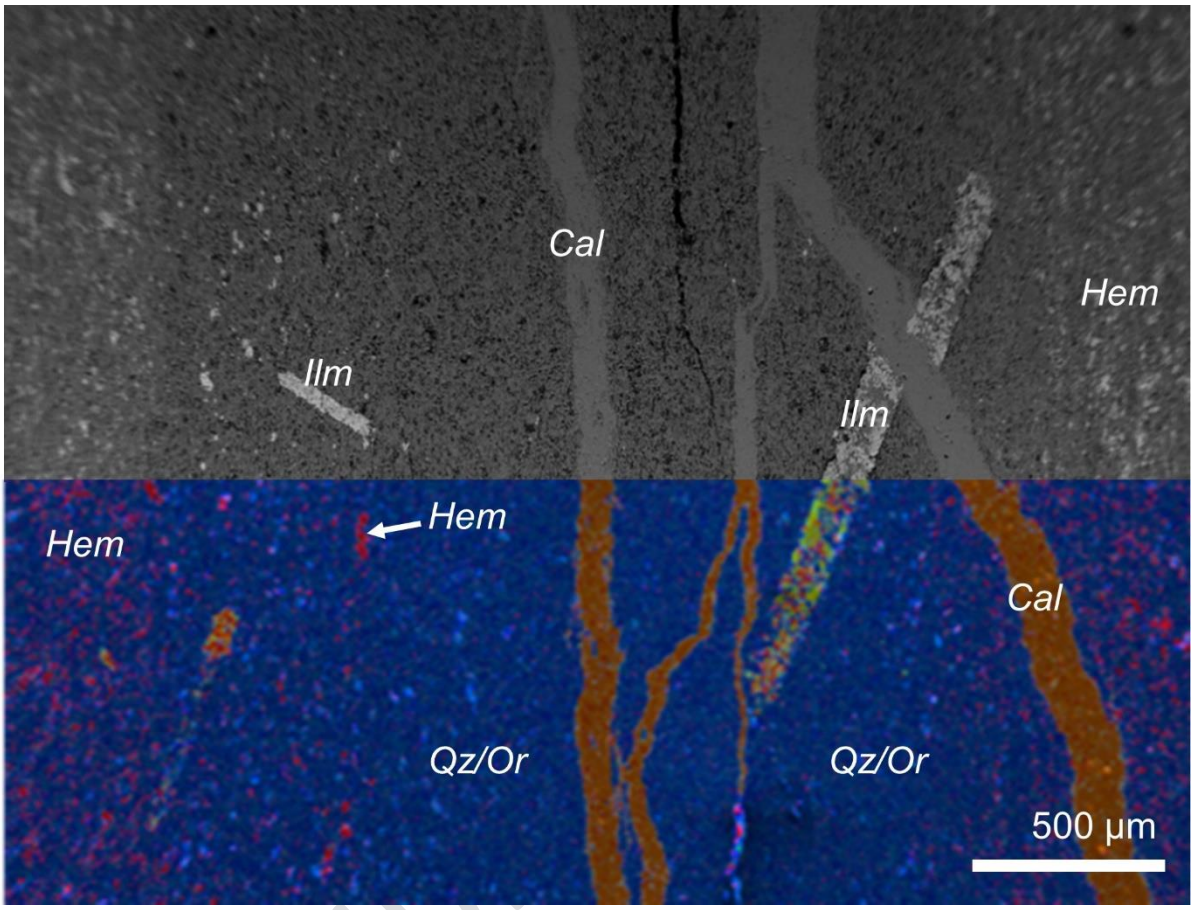

https://doi.org/10.1180/mgm.2025.11 Published online by Cambridge University Press

***Figure 13**: Abundance of specific non-REE trace elements for the dark (red) and light (blue) banding of all print stone samples analysed by LA-ICP-MS, compared against the chemical compositions of eight Post-Archean Australian shales (grey) from Taylor & McLennan (1985).*

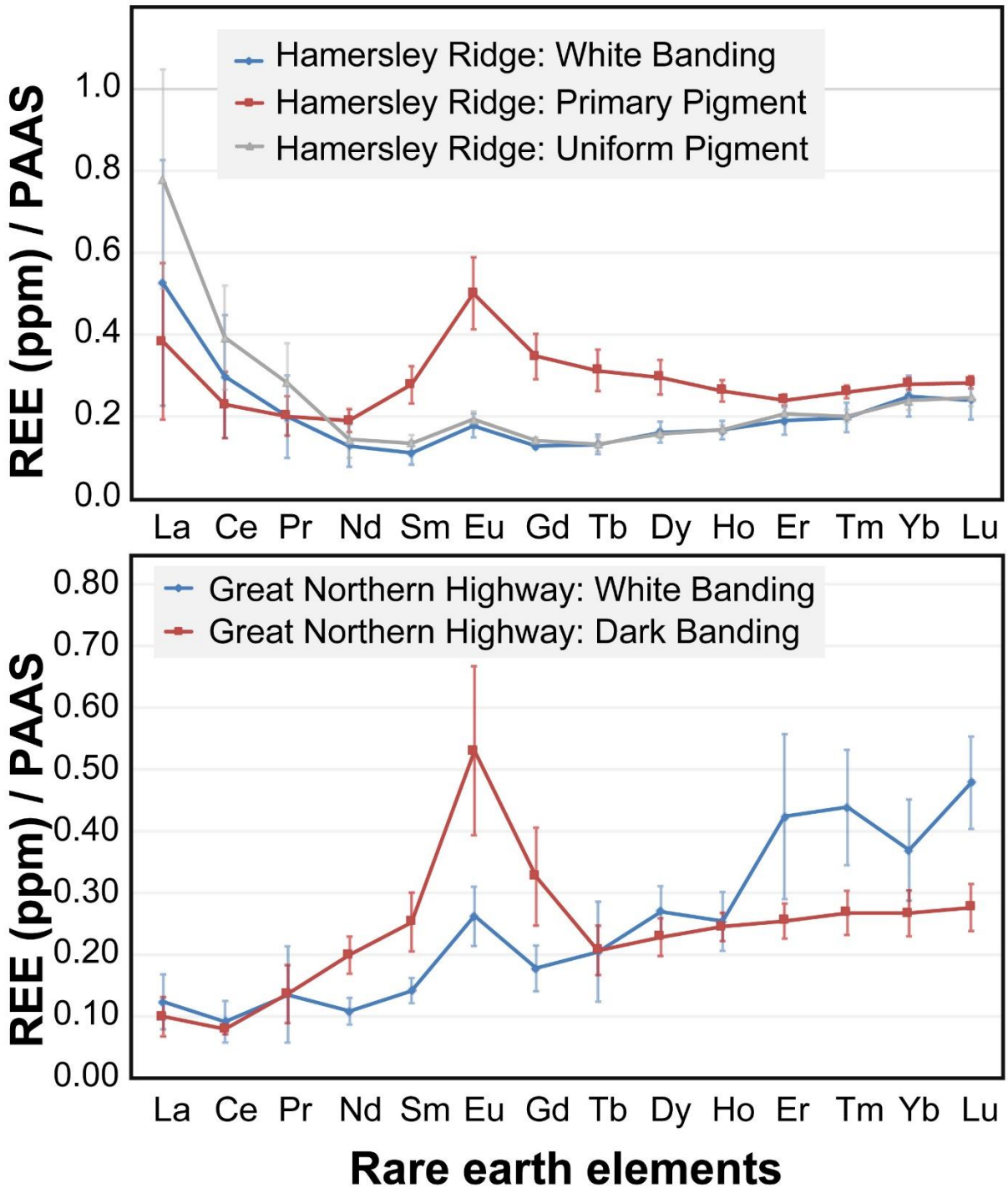

https://doi.org/10.1180/mgm.2025.11 Published online by Cambridge University Press

***Figure 14**: Average abundance of rare earth elements (REEs) normalised to Post Archean Australian Shale (PAAS; Taylor & McLennan, 1985) in the white, primary, and uniform pattern of print stone from Hamersley Ridge and Great Northern Highway. Abundance obtained as the average across three sampling locations. Uncertainty of one standard deviation represented by error bar. Samples analysed: CW2 (top) and PS-L2-1 (bottom).*

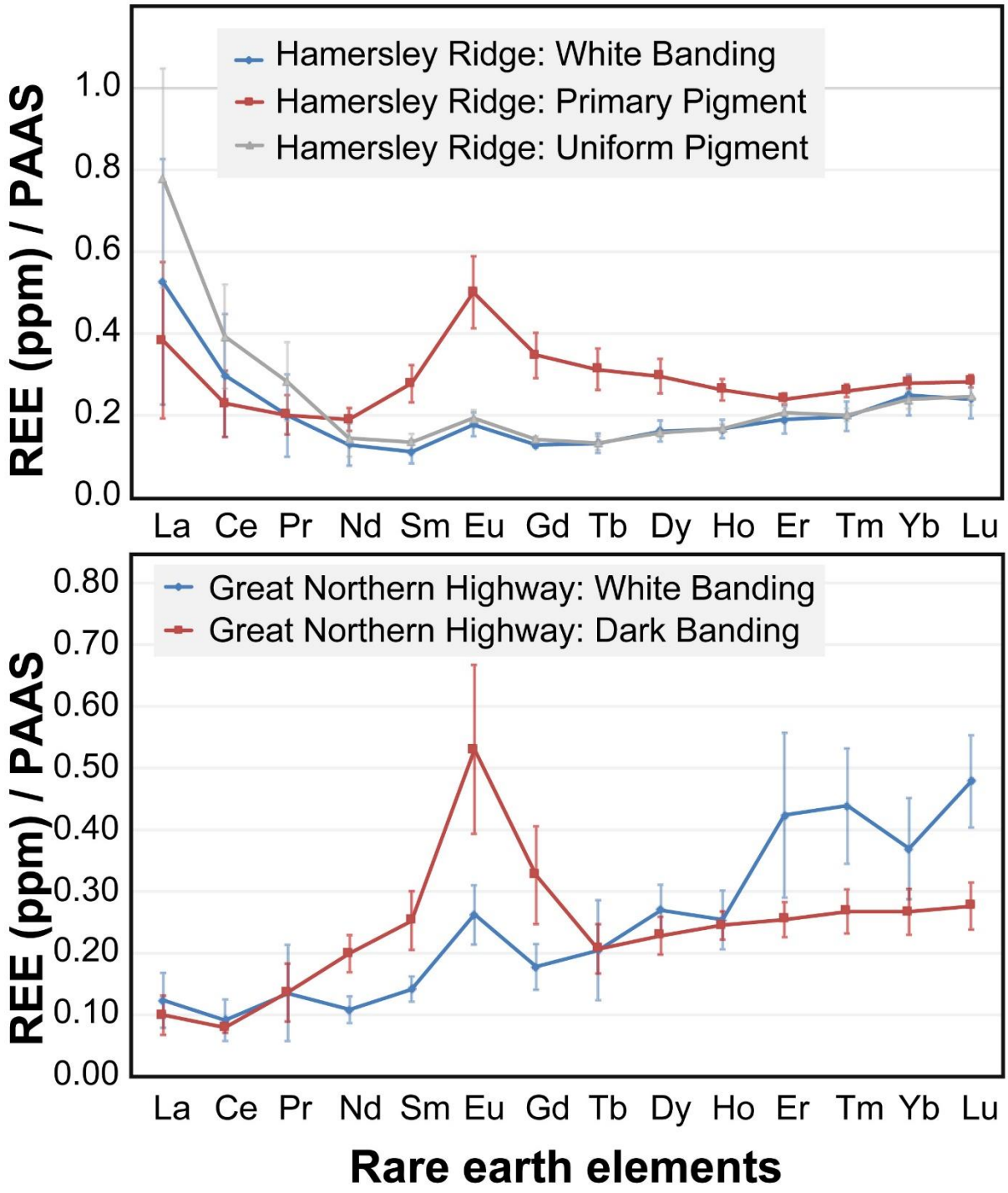

https://doi.org/10.1180/mgm.2025.11 Published online by Cambridge University Press